

Document downloaded from:

<http://hdl.handle.net/10251/193580>

This paper must be cited as:

Hernández-Soto, M.; Erigoni, A.; Segarra, C.; Rey Garcia, F.; Díaz Morales, UM.; Gianotti, E.; Miletto, I.... (2022). Bifunctional hybrid organosiliceous catalysts for aldol condensation-hydrogenation tandem reactions of furfural in continuous-flow reactor. *Applied Catalysis A General*. 643:1-12. <https://doi.org/10.1016/j.apcata.2022.118710>



The final publication is available at

<https://doi.org/10.1016/j.apcata.2022.118710>

Copyright Elsevier

Additional Information

# Bifunctional Hybrid Organosiliceous Catalysts for Aldol Condensation – Hydrogenation Tandem Reactions of Furfural in Continuous-Flow Reactor

M. C. Hernández-Soto,<sup>1</sup> A. Erigoni,<sup>1</sup> C. Segarra,<sup>1</sup> F. Rey,<sup>1</sup> U. Díaz,<sup>1\*</sup> E. Gianotti,<sup>2</sup> I. Miletto,<sup>3</sup> M. Pera-Titus<sup>4,5\*</sup>

<sup>1</sup> *Instituto de Tecnología Química, Universitat Politècnica de València-Consejo Superior de Investigaciones Científicas, Avenida de los Naranjos s/n, E-46022, Valencia, Spain*

<sup>2</sup> *Department for the Sustainable Development and Ecological Transition, Università del Piemonte Orientale, Piazza Sant'Eusebio 5, Vercelli, Italy*

<sup>3</sup> *Department of Science and Technological Innovation, Università del Piemonte Orientale, V. T. Michel 11, Alessandria, Italy*

<sup>4</sup> *Eco-Efficient Products and Processes Laboratory (E2P2L), UMI 3464 CNRS – Solvay, 3966 Jin Du Road, Xin Zhuang Ind. Zone, 201108 Shanghai, China*

<sup>5</sup> *Cardiff Catalysis Institute, School of Chemistry, Cardiff University, Main Building, Park Place, Cardiff CF10 3AT, UK*

\*Corresponding author: [udiaz@itq.upv.es](mailto:udiaz@itq.upv.es), [peratitum@cardiff.ac.uk](mailto:peratitum@cardiff.ac.uk)

---

## Abstract

A series of organic-inorganic hybrid bifunctional organosiliceous catalysts with accessible pendant amine groups as single basic sites (such as propylamine, diethylamine, pyrrolidine) and Pd nanoparticles was prepared from suitable synthesis processes. Pd/MCM-41 silica decorated with propylamine groups was highly active and selective for the single-reactor tandem aldol condensation/crotonization reaction between furfural with methyl isobutyl ketone, followed by hydrogenation, to access renewable biosolvent and biofuel precursors in the branched alkane range at mild temperature (80-100 °C). The catalyst was characterized in detail using XRD, C and N elemental analysis, ICP-OES, TGA/DTA, HR-TEM, N<sub>2</sub> adsorption/desorption at 77 K, solid-state <sup>13</sup>C and <sup>29</sup>Si MAS NMR and FT-IR spectroscopy CO<sub>2</sub> as acid probe. The catalyst was robust when operated in a dual fixed-bed reactor achieving steady 20% furfural conversion for 12 h on stream with preferential formation of 1-(furan-2-yl)-5-methylhexan-3-one.

**Keywords:** Basic hybrid catalysts, Bifunctional Organosilicas, Furfural, Aldol Condensation, Hydrogenation

## 1. Introduction

Furfural (FF) is a valuable platform molecule consisting of an aldehyde group attached to the 2-position of a furan ring that can be directly accessed by the acid-catalyzed dehydration of hexoses and pentoses [1-3]. FF can be used as raw material for the synthesis of chemicals [4-8] and fuels [9-14]. For instance, FF can be selectively converted into furfurylamine by reductive amination with  $\text{NH}_3$  and  $\text{H}_2$ , which is used as intermediate for the synthesis of pesticides, herbicides and pharmaceuticals [15,16]. FF can also be hydrolyzed, oxidized or reduced to generate furfuryl alcohol [17,18], 2-methylfuran and 2-methyltetrahydrofuran [19,20],  $\gamma$ -valerolactone [21], levulinate esters [18] and maleic acid / anhydride [22,23].

FF can be subjected to C-C reactions such as acetalization [24,25], acylation [26], furfural condensation [27], and furan ring alkylation, increasing the molecular complexity. In particular, the aldol condensation/crotonization of FF with ketones (especially acetone) has been used to prepare long-chain liquid fuels and monomers (*e.g.*, dienes). The reaction is commonly catalyzed by alkaline metal oxides based on Mg-Zr, Mg-La, Mg-Al, CaO [28,33], and alkali-exchanged / N-containing zeolites [30,34-36]. Alkaline metal oxides usually suffer from hydration, which can be prevented either by supporting them on mesoporous carbon [37], or by doping with Pd [38]. Acid catalysts, including zeolites, have also been proposed for the reaction, but often require much higher temperatures [39-44]. Acid-base catalysts can be combined with metal nanoparticles (*e.g.*, Pt, Pd), either supported or encapsulated, to engineer aldol condensation-hydrodeoxygenation/hydrogenation reactions in tandem/cascade [44,45] and one-pot/single-reactor fashion [46-51].

Hybrid materials constituted by organic and inorganic fragments linked together by covalent bonds and different levels of porous hierarchy are attractive for engineering multisite catalysts with tunable hydrophilic/hydrophobic properties and low diffusional resistance of reagents, intermediates and products [52,53]. Organocatalytic moieties and metal centers surrounded by organic moieties can be embedded in the framework, with perceptible associated reactivity. In particular, amine moieties (basic centers) can be incorporated in organosilicas and hierarchical zeolites, catalyzing

the aldol condensation of aromatic aldehydes and ketones [54,55], including FF and HMF with acetone [56-58], and the (self)condensation of aldehydes [59,60]. Further developments encompass organic-inorganic hybrids for acid-base catalytic cascades. Corma and coworkers prepared active micro-mesoporous organic-inorganic hybrids constituted of intercalated MWW zeolite layers with bis(triethoxysilyl)benzene hosting pendant amine groups and acid centers in the framework [61]. The resulting materials exhibited high activity in the two-step cascade reaction of benzaldehyde dimethylacetal into benzylidene malonitrile. The same team synthesized acid-base mesoporous hybrid catalysts containing proton sponges and acid groups with high activity in one-pot deacetalization-Knoevenagel condensation and deacetalization-nitroaldol (Henry) reactions [62]. Finally, catalytic cascades combining the oxidation of furfuryl alcohol to FF, followed by aldol condensation with acetone, have been designed over mesoporous silicas incorporating amine groups and Pd nanoparticles [63]. Overall, despite the promising results, catalyst robustness in the presence of FF or HMF is still a challenge for process design, especially at high concentration, which discourages process implementation.

Herein, we prepared a family of bifunctional organosilica catalysts with pendant amine groups as single basic sites (*e.g.*, propylamine, diethylamine, pyrrolidine) and Pd nanoparticles to perform the single-reactor tandem aldol condensation/crotonization reaction of FF with MIBK, followed by hydrogenation of the aldol intermediate, to access a renewable biosolvent and biofuel precursor in the branched alkane range at high yield and mild conditions. The activity and robustness of the catalysts was investigated in batch and continuous dual fixed-bed reactors to devise conditions for upscaling.

## 2. Experimental

### 2.1. Chemicals

(3-Aminopropyl)triethoxysilane (APTES, purity 99 wt.%), N-(2-aminoethyl)-3-(trimethoxysilyl)propylamine (purity 97 wt.%), 2-aminopyrrolidine (purity 98 wt.%) and 3-isocyanatopropyltriethoxysilane (purity 95 wt.%) were used to prepare hybrid catalysts **1**, **2**, and **3**, respectively, with

pendant silylated functional groups. Triethylammonium acetate (1 M) and palladium (II) acetate (purity 97 wt.%) were used to prepare bifunctional hybrid catalyst **4**, incorporating supported Pd nanoparticles. Furfural (purity 99 wt%) and MIBK (purity 99 wt%) were used for catalytic tests. Dry toluene, dichloromethane, ethanol, tetrahydrofuran and ether were used in the different synthesis and reaction processes. All reactants and solvents were purchased from Merck and were used without further purification except for FF, which was distilled before use.

## 2.2. Catalyst preparation

Hybrid catalysts **1**, **2** and **3** propylamine, diethylamine and pyrrolidine pendant groups, respectively, were synthesized on the guidance of a previous report [64]. Briefly, MCM-41 (2 g) was placed in a Schlenk under vacuum at 150 °C for 2 h. Then, dry toluene was added, and the mixture was stirred for 1 h at room temperature. Then, the silyl base precursor (1.3 mmol) was added, i.e. 295 mg for (3-aminopropyl)triethoxysilane (APTES), 297 mg for N-(2-aminoethyl)-3-(trimethoxysilyl)propylamine and 445 mg for (pyrrolidine-3-yl)urea-3-(triethoxysilyl)propylamine), and the resulting mixture was refluxed for 24 h. After this time, the mixture was filtered, and the solid was washed with toluene, dichloromethane and ethanol, and dried overnight at 100 °C.

High pore accessibility and pendant amine groups, acting as active capping agents [65], are known to favor the dispersion of Pd nanoparticles. Bifunctional palladium hybrid organosiliceous catalyst **4**, incorporating supported Pd nanoparticles, was synthesized starting from catalyst **1**, containing propylamine groups. Specifically, catalyst **1** (1.5 g) and triethylammonium acetate (0.47 mmol, 142 mg) were placed in a Schlenk under N<sub>2</sub>. Pd(OAc)<sub>2</sub> (0.15 mmol, 33.7 mg) was dissolved in dry THF (10 mL), and the solution was filtered with a Teflon syringe filter (0.45 μL) and poured into the Schlenk. The resulting mixture was refluxed for 4 h and stirred at room temperature overnight. After this time, the mixture was filtered and the solid was washed with ether and dried for 1 h at room temperature. A qualitative scheme of the different moieties is depicted in [Scheme 1](#).

## 2.3. Catalyst characterization

Elemental analysis (C, N, S and H content) was conducted using a Carlo Erba 1106 elemental analyzer. The Pd composition in catalyst **4** was measured on a Varian 715-ES ICP-Optical Emission spectrometer after dissolution of the solids in HNO<sub>3</sub>/HCl/HF aqueous solution.

Powder X-ray diffraction (XRD) patterns of the different samples were measured on a Philips X'PERT diffractometer equipped with a proportional detector and a secondary graphite monochromator. Data were collected stepwise in the 2° < 2θ < 20° angular region using Cu Kα (λ = 1.54178 Å) radiation. The patterns were indexed using the Joint Committee on Powder Diffraction (JCPDS) database and interpreted using MDI JADE 5.0 software.

N<sub>2</sub> adsorption/desorption isotherms were measured on a Micromeritics ASAP 2010 volumetric adsorption analyzer at -196 °C. The BET specific surface area was calculated from the N<sub>2</sub> adsorption data in the relative pressure range from 0.04 to 0.2. The total pore volume was measured from the amount of N<sub>2</sub> absorbed at P/P<sub>0</sub> = 0.99. The external surface area and micropore volume were measured using the *t*-plot method in the *t* range from 3.5 to 5. The average pore size and pore size distribution were measured using the Barret-Joyner-Halenda (BJH) method on the adsorption branch of the N<sub>2</sub> isotherms.

The size distribution of Pd nanoparticles was measured by HR-TEM using a JEOL, JEM-2100 (200 kV) microscope equipped with a LaB<sub>6</sub> electron gun. The images were analyzed by ImageJ software. The particle size distributions of Pd nanoparticles were measured over 148 particles collected in six clichés. In the analyses, we assumed that the metal particles are spherical in shape and we took explicitly into account the density ratio between the oxide and metal phases. The average particle size (surface weighted,  $d_p[3,2]$ ) was estimated from the particle size distribution using the expression

$$d_p[3,2] = \frac{\sum_{i=1}^{i=n} d_{p,i}^3 n_i}{\sum_{i=1}^{i=n} d_{p,i}^2 n_i} \quad (1)$$

Thermal gravimetric analysis was conducted on a Mettler Toledo TGA/SDTA 851E analyzer using an air stream.

FTIR spectra of self-supporting pellets were collected under vacuum conditions (residual pressure  $<10^{-5}$  mbar) using a Bruker Equinox 55 spectrometer equipped with a pyroelectric detector (DTGS type) with a resolution of  $4\text{ cm}^{-1}$ .  $\text{CO}_2$  was adsorbed at room temperature on the samples outgassed at  $150\text{ }^\circ\text{C}$  using specially designed cells permanently connected to a vacuum line to perform adsorption-desorption *in situ* measurements. FTIR spectra were normalized with respect the pellet weight and, whenever specified, were reported in difference-mode by subtracting the spectrum of the sample in vacuum from the spectrum of the adsorbed molecules.

Solid-state MAS NMR spectra were recorded at room temperature under magic angle spinning (MAS) in a Bruker AV-400 spectrometer. The single pulse  $^{29}\text{Si}$  spectra were acquired at 79.5 MHz with a 7 mm Bruker BL-7 probe, using pulses of  $3.5\text{ }\mu\text{s}$  corresponding to a flip angle of  $3/4\pi$  radians and a recycle delay of 240 s. The  $^1\text{H}$  to  $^{13}\text{C}$  cross polarization (CP) spectra were acquired by using a  $90^\circ$  pulse for  $^1\text{H}$  of  $5\text{ }\mu\text{s}$ , a contact time of 5 ms, and a recycle of 3 ms. The  $^{13}\text{C}$  spectra were recorded with a 7 mm Bruker BL-7 probe and at a sample spinning rate of 5 kHz.  $^{13}\text{C}$  and  $^{29}\text{Si}$  were referred to adamantane and tetramethylsilane, respectively.

#### 2.4. Catalytic tests in batch reactor

The aldol condensation-crotonization and single-reactor tandem aldol condensation/crotonization-hydrogenation reactions were carried out in a stainless steel reactor (Tynyclave 10 mL, Büchi) equipped with a heater, mechanical stirrer and gas supply system (batch mode). In a typical test, the reactor was charged with FF (1 mmol), MIBK (2 mmol), toluene (0.5 g) and the catalyst (10 mol<sub>N</sub>% with respect to FF). The reactor was heated to  $80\text{ }^\circ\text{C}$  for 24 h (aldol condensation step) and further at  $80\text{ }^\circ\text{C}$  for 8-24 h at 5 bar  $\text{H}_2$  (hydrogenation step).

In each experiment, the FF conversion (FF = limiting reactant), selectivity and yield of each product, as well as the carbon balance (CB), were defined as follows (eqs 2-5)

$$\text{FF conversion} = 1 - \frac{n_{\text{FF}}}{n_{\text{FF}}^0} \times 100 \quad (2)$$

$$\text{Selectivity}_i = \frac{n_i}{n_{\text{FF}}^0 - n_{\text{FF}}} \times 100 \quad (3)$$

$$\text{Yield}_i = \frac{n_i}{n_{\text{FF}}^0} \times 100 \quad (4)$$

$$\text{CB}_{\text{FF}} = \frac{\sum n_i + n_{\text{FF}}}{n_{\text{FF}}^0} \times 100 \quad (5)$$

where  $n_{\text{FF}}^0$  and  $n_{\text{FF}}$  refer to the initial and final mole number of FF, respectively, and  $n_i$  is the mole number of product  $i$ .

The turnover number (TOF) was measured as the derivate of the time-evolution of the mole number of product  $i$  by the mole number of N as follows

$$\text{TOF}_i = \frac{1}{n_{\text{N}}} \left. \frac{dn_i}{dt} \right|_{t=0} \quad (6)$$

where  $n_{\text{N}}$  is the number of moles of N in the reactor.

### 2.5. Experiments in dual fixed-bed reactor

A series of catalytic tests was conducted in a fixed-bed reactor (stainless steel, i.d. 6 mm) (see scheme of the setup in [Figure S1](#)). The gas and liquid were simultaneously co-added at the reactor inlet using a thermal mass flow controller ( $\pm 1\%$  accuracy, EL-Flow Bronkhorst) and a syringe pump ( $\pm 5\%$  accuracy, KDScientific), respectively. The temperature was regulated using a homemade PID controller ( $\pm 1$  °C accuracy).

The downflow fixed-bed reactor was loaded from the bottom to the top in three layers. The first layer (bottom) of 200- $\mu\text{m}$  SiC ensured the positioning of the catalyst(s) within the isothermal zone in the reactor. The catalyst (300 mg) was loaded as second layer followed by a third layer of 200- $\mu\text{m}$  SiC that facilitated the feed mixing and brought it up to the reaction temperature. The different layers were separated using glass wool.



The reactor outlet was cooled down to room temperature and liquid samples were recovered every hour. The weight-hourly space velocity of the reactor referred to 1-octanol ( $\text{WHSV}_{\text{FF}}$ ) was defined as follows

$$\text{WHSV}_{\text{FF}} (\text{h}^{-1}) = \frac{F_{\text{FF}}^0 (\text{mL} \cdot \text{h}^{-1})}{W(\text{g})} \rho_{\text{FF}} (\text{g} \cdot \text{mL}^{-1}) \quad (7)$$

where  $F_{\text{FF}}^0$  is the FF liquid flowrate at the reactor inlet (range 1.0-2.0  $\text{mL} \cdot \text{h}^{-1}$ ),  $W$  is the catalyst loading (300-600 mg), and  $\rho_{\text{FF}}$  is the FF density ( $1.16 \text{ g} \cdot \text{mL}^{-1}$ ).

The FF conversion, selectivity and yield of each product, as well as the carbon balance (CB), at the outlet of the reactor were defined using the following expressions (eqs 8-11)

$$\text{FF conversion} = 1 - \frac{F_{\text{FF}}}{F_{\text{FF}}^0} \times 100 \quad (8)$$

$$\text{Selectivity}_i = \frac{F_i}{F_{\text{FF}} - F_{\text{FF}}^0} \times 100 \quad (9)$$

$$\text{Yield}_i = \frac{F_i}{F_{\text{FF}}^0} \times 100 \quad (10)$$

$$\text{CB}_{\text{FF}} = \frac{\sum F_i + F_{\text{FF}}}{F_{\text{FF}}^0} \times 100 \quad (11)$$

where  $F_{\text{FF}}^0$  and  $F_{\text{FF}}$  refer to the initial and final FF molar flow, respectively, and  $F_i$  is the molar flow of product  $i$ .

In a first set of experiments, the aldol condensation/crotonization reaction was carried out at 80 °C for 12 h using 4.8 wt% of FF, and 1:2 FF/MIBK and 1:9 MIBK/toluene molar ratios. Next, catalysts **1** and **4** were combined in a dual fixed-bed reactor configuration, so that catalyst **4** was placed at the bottom of catalyst **1**, and the reaction was carried out at the same reaction conditions. Two catalytic tests conducted at a constant  $\text{WHSV}$  of  $0.35 \text{ h}^{-1}$ , but varying the FF liquid flowrate and catalyst loading in the reactor, reveal no remarkable differences in FF conversion, pointing out the absence of mass transfer effects on the conversion curves. This observation is consistent with the Mears criterion (see SI), confirming a lack of mass transfer effects in our reactor, and confirming accordingly a plug-flow hydrodynamic regime.

## 2.6. Analysis of reaction media

After the reaction, the mixture was centrifuged to separate the solution from the catalyst. The concentration of the non-reacted FF and MIBK, as well as the reaction products, were identified and analyzed by liquid  $^1\text{H}$  NMR using  $\text{CDCl}_3$  as deuterated solvent. Each compound was characterized using several descriptors including the chemical shift, spin multiplicity, coupling constants, and integration. The  $^1\text{H}$  NMR spectra were recorded on a 400 MHz Bruker spectrometer and quantification was carried out using 4-chlorotoluene as internal standard, which was added to the reacted solution after analysis. Examples of crude  $^1\text{H}$  NMR spectra of the reaction products obtained in the aldol condensation reaction between FF and MIBK, and single-reactor aldol condensation reaction of FF and MIBK followed by hydrogenation, in batch reactor, are provided in [Figures S2](#) and [Figure S3](#), respectively.

The FF conversion was measured using the aldehyde signal  $-\text{CHO}$  at 9.7 ppm, while the yield of the aldol condensation product (ALD-1) using the characteristic  $-\text{CH}-$  band at 6.6 ppm belonging to the furan ring. The yield of the hydrogenated products F-ALD-1-ON, F-ALD-1-OL and F-ALD-1-AN was measured using the  $-\text{CH}_2-$  signal next to the furan ring at 3.0 ppm, the  $-\text{CH}-$  signals of the furan ring at 6.4 ppm and the  $-\text{OH}$  signal at 4.7 ppm, respectively.

### 3. Results and Discussion

#### 3.1. Catalytic tests in batch reactor

##### 3.1.1. Catalytic performance of amine-functionalized catalysts

In a first series of experiments, we explored the effect of the amine group (i.e. propylamine, diethylamine, pyrrolidine) on the performance of the different hybrid catalysts in the aldol condensation/crotonization reaction of FF with MIBK at 80 °C for 24 h in the absence of solvent. [Table 1](#) lists the main properties of the catalysts. In all cases, the reaction leads to an intermediate product that dehydrates spontaneously to form 1-(furan-2-yl)-5-methylhex-1-en-3-one (ALD-1) ([Scheme 2](#)). Interestingly, ALD-2a,b by-products, which are also generated over Brønsted acid catalysts (e.g., SAPO-5 zeolites), are not formed in our catalytic system [\[51\]](#), as well as secondary

condensation products. Among the different catalysts, catalyst **1** exhibits the highest yield (75%), which is somehow unexpected according to the pKa of the amine groups, the lowest value corresponding to catalyst **2** (Figure 1A1). This observation suggests that steric effects around the amine groups in mesochannels dominate the catalytic activity [66]. Moreover, longer amines can exhibit higher interaction with the silica surface, decreasing the catalytic activity [67]. Details on the morphology and pore architecture of the catalysts is provided in section 3.3.

Given these results, we carried out additional tests using catalyst **1** as a function of the FF/MIBK molar ratio in the absence of solvent. The ALD-1 yield increases slightly with the FF/MIBK molar ratio from 70% at 1:8 ratio to 77% at 1:4 ratio, but decreases further until 52% at 1:2 ratio (Figure 1A2). In view of these results, a 1:4 ratio was further used to optimize the reaction conditions. The turnover frequency for ALD-1 ( $\text{TOF}_{\text{ALD-1}}$ ), measured with respect to the molar number of N from the kinetic profile (Figure 1B), is about  $4.0 \text{ h}^{-1}$ .

### 3.1.2. Optimization of catalytic performance for catalyst **1**

We further optimized the reaction conditions for the aldol condensation of FF with MIBK over catalyst **1**. We screened different solvents to promote the solubilization of FF and catalyst dispersion, such as ethanol, toluene and acetonitrile. Poor homogenization was achieved using ethanol and acetonitrile. On the contrary, toluene allowed an optimal solubilization of FF in the reaction system, being selected as more suitable solvent for the process.

Table 2 lists the results obtained both in the absence of solvent and in toluene at 80-100 °C and 1:2 FF/MIBK molar ratio at variable catalyst loading. In all cases, ALD-1 was obtained as sole product with 100% selectivity. In the absence of solvent and 80 °C, the ALD-1 yield is 56% using 5 mol<sub>N</sub>% catalyst (entry 1). Addition of 0.5 g of toluene decreases only slightly the ALD yield to 52% (entry 2), and decreases further to 30% using 1.0 g of toluene (entry 3), suggesting an apparent reaction order with respect to FF higher than zero. In all cases, the carbon balance is higher than 95%. Using 0.5 or 1.0 g of toluene, the ALD-1 yield rises with the catalyst loading

from 5 mol<sub>N</sub>% to 10 mol<sub>N</sub>% with respect to FF (compare entries 2 and 4 or 6, and entries 3 and 5). Finally, increasing the temperature from 80 °C to 100 °C using 10 mol<sub>N</sub>% catalyst with respect to FF, almost complete ALD-1 yield is achieved regardless of the toluene volume (compare entries 4 or 6 and 7, and entries 5 and 8, respectively).

### 3.1.3. Catalyst stability

Given the results at optimized reaction conditions, we explored the stability of catalyst **1** in two consecutive catalytic runs (see also Table 2). A large decline of the FF conversion is observed after the first run and becomes almost suppressed in the absence of solvent (entry 1). This decline is attributed to the formation of oligomers on the catalyst surface during the first run blocking the propylamine sites. Indeed, the catalyst color evolves from white to orange-brown after the first run. Different solvents (*i.e.* acetone, toluene, DMSO) and experimental conditions were employed to wash and recover the catalyst after the first run using toluene as solvent. At 80 °C and 5 mol<sub>N</sub>% of catalyst **1**, the ALD-1 yield is lower than 15% after washing with acetone (entries 2-3). Likewise, the ALD-1 yield is only 32% after the second run compared to the initial value (74%) using 10% mol<sub>N</sub>% of catalyst (entry 5). Additional tests using toluene and DMSO at 80 and 100 °C using 5 mol<sub>N</sub>% of catalyst also result in a much lower ALD-1 yield (<25%) (entries 4,6,7,8), pointing out a high stability of surface deposits. Detailed characterization of surface deposits is provided in section 3.3.5.

### 3.1.4. Single-reactor aldol condensation/crotonization + hydrogenation reactions

The hybrid Pd-based catalyst **4** was tested in a single-reactor process consisting of the aldol condensation/crotonization of FF with MIBK, followed by hydrogenation of the aldol intermediate (ALD-1) at 100 °C. Overall, three hydrogenated products are generated: 1-(furan-2-yl)-5-methylhexan-3-one (F-ALD-1-ON), 1-(furan-2-yl)-5-methylhex-1-en-3-ol (F-ALD-1-OL) and 1-(furan-2-yl)-5-methylhexan-3-ol (F-ALD-1-AN) (Scheme 3). Interestingly, at such low temperatures, tetrahydrofuran products are observed within the limits of the experimental error.

A series of catalytic tests were performed to assess the influence of the operation variables on the FF conversion and selectivity towards the different hydrogenated products (Table 3). First, the reaction was carried out at 80 °C for both steps (entry 1). The FF conversion reaches 75% with F-ALD-1-AN and F-ALD-1-ON yields of 44% and 21%, respectively. By halving the catalyst loading (entry 2), the FF conversion declines to 48% with preferential formation of F-ALD-1-ON (23% yield). By decreasing the FF/MIBK molar ratio from 1:2 to 1:4 (entry 3 vs. entry 2), the FF conversion raises to 65% with ALD-1-ON and F-ALD-1-AN yields of 30% and 29%, respectively. When the reaction is carried out in a single step by adding H<sub>2</sub> together with FF and MIBK (entry 4), high selectivity towards the most reduced product, *i.e.* F-ALD-1-AN, is obtained with 38% yield at 57% FF conversion with no formation of furfuryl alcohol.

After this initial screening, the temperature of both steps was raised from 80 °C to 100 °C (entry 5), resulting in no major change in the FF conversion (80% vs. 75% in entry 1). However, a drastic change in selectivity is observed resulting in 63% yield of F-ALD-1-ON in detriment of F-ALD-1-AN. A catalytic run was performed in the absence of solvent at 1:6 FF/MIBK molar ratio (entry 6). Although almost full FF conversion is achieved, the reaction displays similar yield of F-ALD-1-ON and F-ALD-1-AN (*i.e.* 44% and 47%, respectively). Finally, a catalytic run was carried out at 100 °C and 24 h, giving almost full FF conversion and 82% yield of F-ALD-1-AN (entry 7). In all cases, no formation of THF-derivatives is observed opposing earlier observations using acid zeolites, occurring at higher temperature (140-180 °C) [51]. Also noteworthy, catalyst **1** can be operated at much lower temperature compared to earlier reported basic catalysts for the aldol condensation of FF and MIBK (130 °C for both CaO [32,33] and Cs@GO/UiO [68]). These results pave the way to a thorough optimization under flow in a fixed-bed reactor as described below.

### 3.2. Catalytic activity tests in dual fixed-bed reactor

The results above point out the feasibility of a batchwise single-reactor tandem process for the aldol condensation/crotonization reaction of FF with MIBK, followed by hydrogenation. However, even in the presence of a solvent (*i.e.* toluene), catalyst **1** deactivates fast during the first run and can be hardly recycled. To promote the catalyst stability during the reaction, catalyst **1** was tested in a fixed-bed reactor operated in continuous mode (see Experimental section in the SI for details)

(Figure S4). The FF conversion remains stable during 12 h on stream, but the catalyst stability depends upon the catalyst loading and residence time. The optimal amount of catalyst **1** is about 0.3 g, whereas a higher catalyst amount results in an unstable FF conversion and mass transfer limitations (not shown). The flowrate was set at the range 1.0-1.5 mL/h, affording a steady-state FF conversion about 15% at 100% ALD-1 selectivity.

Next, we combined catalysts **1** and **4** in a dual fixed-bed reactor (see also Experimental section in the SI for details) (Figure 2). First, we built a reactor including 150 mg of catalyst **1** and 150 mg of catalyst **4** (WHSV = 0.35 h<sup>-1</sup>). Introducing H<sub>2</sub> at 80 °C and 2 mL(STP)/min H<sub>2</sub> flowrate promotes catalyst deactivation compared to a control test in a fixed-bed with 300 mg of catalyst **1** (WHSV = 0.35 h<sup>-1</sup>). At the same H<sub>2</sub> flowrate, an increase of temperature from 80 °C to 100 °C does not promote appreciably the FF conversion. Next, we built a reactor including 300 mg of catalyst **1** and 150 mg of catalyst **4** (WHSV = 0.23 h<sup>-1</sup>). Introducing H<sub>2</sub> at 100 °C and 2 mL(STP)/min H<sub>2</sub> flowrate promotes only slightly the FF conversion during 12 h on stream. At these conditions, decreasing the H<sub>2</sub> flowrate to 1.0-1.5 mL(STP)/min promotes the FF conversion to 20%, and keeps almost constant during 12 h on stream.

At the latter conditions (WHSV = 0.23 h<sup>-1</sup>), we also measured the evolution of the selectivity to the different hydrogenated products as a function of the time of stream, and plotted the selectivity-conversion curves, at a H<sub>2</sub> flowrate to 1.0-1.5 mL(STP)/min (Figure 3). The hydrogenated product ALD-1-ON is preferentially generated with a decreasing trend with the time of stream in detriment of ALD-1, especially at 1.5 mL(STP)/min H<sub>2</sub> flowrate while products ALD-1-OL and ALD-1-AN show selectivity lower than 10% (Figure 3B1-B2).

### 3.3. Characterization of catalysts **1** and **4**

The catalytic results for single-reactor tandem aldol condensation of FF with MIBK, followed by hydrogenation, in dual-type fixed bed reactor point out a high and **steady**-stable catalytic performance. In light of these results, we explored in detail the structure of catalysts **1** and **4** among the different hybrid catalysts prepared in this study, and their evolution during the reactions.

### 3.3.1. Catalyst architecture

The low-angle XRD patterns of catalysts **1-3** reveal in all cases the presence of three reflections centered at  $2\theta = 2.4^\circ$ ,  $3.8^\circ$  and  $4.8^\circ$  that can be assigned to (100), (110) and (200) planes, pointing out that the hexagonal symmetry of MCM-41 keeps unchanged after grafting (Figure 4). However, a slight shift to higher angles with concomitant decrease of intensity is apparent for the first reflection, suggesting a smaller pore diameter as confirmed by analysis of the textural properties (see below). The three reflections are still observed after incorporation of Pd nanoparticles (catalyst **4**), matching the pattern of catalyst **1**. This observation points out that Pd incorporation does not affect the integrity of the mesoporous architecture. In particular, no major change is observed for the main reflection of MCM-41 after Pd deposition.

### 3.3.2. Porous structure

The textural properties of catalysts **1-4** were studied by  $N_2$  adsorption/desorption at 77 K and were compared to those of the pristine MCM-41 support (Figure 5A and Table 1). In all cases, the isotherms exhibit a Type IV pattern with a characteristic H1-type hysteresis loop which is indicative of the presence of mesopores [69]. The incorporation of propylamine moieties and Pd nanoparticles induces a shift of the inflection point in the  $P/P_0$  range between 0.2-0.4. The specific surface area is similar for all catalysts and close to the value measured on the support ( $1064 \text{ m}^2 \text{ g}^{-1}$ ), except for catalyst **4** with *ca.* 10% reduction. The pore volume declines from  $0.81 \text{ cm}^3 \text{ g}^{-1}$  for pristine MCM-41 to  $0.43\text{-}0.55 \text{ cm}^3 \text{ g}^{-1}$  for catalysts **1-3**, suggesting a homogeneous distribution of propylamine moieties in the mesochannels (Table 1). The pore volume of catalyst **4** ( $0.13 \text{ cm}^3 \text{ g}^{-1}$ ) is much lower than the value measured on catalyst **1** ( $0.47 \text{ cm}^3 \text{ g}^{-1}$ ), which can be explained by partial pore occupancy of Pd nanoparticles inside the mesochannels, avoiding  $N_2$  adsorption.

Despite the marked decline of the pore volume, the presence of amine moieties and Pd nanoparticles in catalysts **1-3** only affects slightly the average pore size, decreasing slightly from 2.7 nm for the parent MCM-41 to 2.2-2.5 nm for catalysts **1-3** (Figure 5B). The smallest average pore size is observed for cat-

alyst **3** (2.2 nm), matching the shift to higher angles observed in the XRD patterns (**Figure 4**). The introduction of either voluminous pendant amine moieties (catalyst **3**), or Pd nanoparticles (catalyst **4**), results in a broader pore size distribution and lower internal free pore volume. The average pore size of catalyst **4** keeps almost unchanged compared to the value measured for catalyst **1** (2.5 nm vs. 2.4 nm). This observation is consistent with the lack of change for the main reflection of MCM-41 in the XRD patterns after Pd deposition (**Figure 4**).

### 3.3.3. *Distribution of amine groups*

The organic content of the hybrid catalysts **1-3** was measured by elemental analysis. **Table 1** lists the C and N content and weight percentage of organic moieties. The organic content evolves from 4.4 wt% for catalyst **1** to 10.4 wt% for catalyst **3**, which is consistent with the molecular weight of the organic moieties. Nonetheless, catalyst **4**, directly issued from catalyst **1** but incorporating Pd, exhibits an unexpectedly higher organic content (10 wt%), which is likely attributed to the presence of adsorbed triethylammonium acetate from the palladium precursor incorporated during the impregnation process (see more details below).

Further TGA/DTA analysis was conducted to gain insight into the organic content and thermal stability of catalysts **1-3** (**Figure 6**). The first weight loss appears in the range 90-150 °C which is associated to desorption of physisorbed water, while the second weight loss in the range 200-400 °C is ascribed to decomposition of organic moieties. A progressive weight loss at temperatures above 500 °C is also visible due to dehydroxylation ascribed to condensation of external silanol groups [70].

To assess the integrity of the organic moieties in the hybrid catalysts and covalent insertion of the silylated basic precursor, catalysts **1-4** were characterized by solid-state  $^{13}\text{C}$  CP/MAS NMR spectroscopy (**Figure 7**). The  $^{13}\text{C}$  NMR spectra show typical bands that are attributed to silylated derivatives, confirming the integrity of the organic moieties. Specifically,  $^{13}\text{C}$  NMR chemical shifts due to aliphatic carbon atoms appear in the range 0-70 ppm for catalysts **1-3** [71], while the



C=O band of catalyst **3** appears at 160 ppm [72]. The solid-state  $^{13}\text{C}$  CP/MAS NMR spectrum of catalyst **4** evidences the stability of propylamine moieties after Pd incorporation, keeping the original chemical shifts of catalyst **1**. However, additional bands appear in the range 0-60 ppm together with a characteristic C=O band at 179 ppm that is ascribed to triethylammonium acetate from the palladium precursor incorporated during the impregnation process [72], confirming our initial hypothesis. The solid-state  $^{29}\text{Si}$  MAS NMR spectra corroborate the grafting outcome for catalysts **1-4** (see ESI, Figure S5), showing characteristic T-type bands that can be assigned to Si-C species. This observation confirms the covalent incorporation of pendant organosilylated groups on the silica surface.

The mono- and bifunctional hybrid catalysts with the best catalytic performance, catalysts **1** and **4** (see catalytic section below), were characterized by FTIR spectroscopy. The FTIR spectra of catalyst **1**, catalyst **4** and the pristine MCM-41, outgassed at 150 °C to remove physisorbed water, are reported in Figure S6. MCM-41 shows a narrow band at 3740  $\text{cm}^{-1}$  and a broad band at *ca.* 3540  $\text{cm}^{-1}$  that are ascribed to the O-H stretching mode of isolated Si-OH and Si-OH groups interacting *via* H-bonds, respectively. Upon grafting of propylamine (catalyst **1**), both bands become less intense, confirming the grafting of Si-OH groups. In parallel, new bands appear at 3370 and 3300  $\text{cm}^{-1}$  that are attributed to asymmetric and symmetric N-H stretching modes belonging to amine groups. New bands are also visible at 2966, 2930 and 2880  $\text{cm}^{-1}$  that are attributed to C-H asymmetric and symmetric stretching modes of  $\text{CH}_3$  and  $\text{CH}_2$  groups, respectively, of the alkyl chain in pendant propylamine moieties. In the low frequency region, the bands between 1650 and 1500  $\text{cm}^{-1}$  are ascribed to the N-H bending mode of amine groups, while the signal at 1630  $\text{cm}^{-1}$  is related to the bending mode of isolated  $\text{NH}_2$  groups [73,74]. Besides, C-H bending modes are visible below 1500  $\text{cm}^{-1}$ . After loading Pd nanoparticles (catalyst **4**), all the bands due to N-H and C-H vibration modes are still visible, confirming that the protocol used to impregnate Pd nanoparticles does not affect the original amine groups in catalyst **1**.

To gain insight into the basic species (amine groups) and confirm their accessibility after Pd impregnation, catalysts **1** and **4** were further characterized by FTIR spectroscopy, using CO<sub>2</sub> as probe molecule adsorbed at room temperature (Figure 8). In both cases, a band at 2340 cm<sup>-1</sup> ascribed to linearly adsorbed CO<sub>2</sub> is observed which is red-shifted with respect to the gas-phase value (2349 cm<sup>-1</sup>) [75]. The band intensity declines at lower CO<sub>2</sub> pressures (curves a-d), and completely vanishes after outgassing the samples at room temperature (curves e), suggesting weak interaction of CO<sub>2</sub> with the surface. This band is also visible when CO<sub>2</sub> is adsorbed on pristine MCM-41 (Figure 8A curve  $\alpha$ ) pointing out an interaction between CO<sub>2</sub> and surface Si-OH groups. A negative band at *ca.* 3740 cm<sup>-1</sup> and a broad absorption band at *ca.* 3250 cm<sup>-1</sup> appear simultaneously in all FTIR spectra, which can be explained by the interaction between CO<sub>2</sub> and isolated Si-OH groups driven by H-bonding.

CO<sub>2</sub> adsorption also shows negative bands (3370 and 3310 cm<sup>-1</sup>) due to interaction between CO<sub>2</sub> and NH<sub>2</sub> groups, together with a series of positive bands in the low frequency region (<1700 cm<sup>-1</sup>) that do not completely vanish by outgassing the samples at room temperature (curves e). This observation points out a strong interaction between CO<sub>2</sub> and the amine groups due to the formation of carbamate species (see scheme in Figure 8A). The band intensity is lower for catalyst **4**, pointing out that Pd nanoparticles does not affect the accessibility of amine groups on the silica surface. Additional bands at 1630 and 1495 cm<sup>-1</sup> can be attributed to bending modes of propylammonium species, whereas the bands at 1555 and 1430 cm<sup>-1</sup> are ascribed to asymmetric and symmetric stretching modes of formate anions [76].

#### 3.3.4. Pd dispersion

Bright- and dark-field HR-TEM micrographs recorded on catalyst **4** show high dispersion of Pd nanoparticles over MCM-41 with a narrow size distribution centered at 2.0-2.5 nm and a maximum value of 4.5 nm, but without evidence of Pd macro-aggregates (Figure 9). Noteworthy, the average particle size of Pd nanoparticles matches the diameter of the mesoporous channels of MCM-41, suggesting that most of

Pd nanoparticles are encapsulated. This observation is consistent with the marked decline of the pore volume of catalyst **4** compared to catalyst **1** after Pd loading (**Figure 5A**). To a minor extent, few larger particles are located on the external surface of the support. The Pd loading in the catalyst is 0.8 wt% as inferred from ICP-OES (**Table 1**), resulting in a Pd/N molar ratio of 0.10. Although Pd nanoparticles are expected to be located near the amine groups, this observation points out that most of the amine groups are free from Pd and can behave as active basic centers.

### 3.3.5. *Nature of deposits after reaction*

To further rationalize the nature of the deposits after reaction, the spent catalyst **1** after the first catalytic run (**Table 1** entry 7) was subjected to comprehensive characterization. The XRD pattern exhibits the characteristic reflections of the pristine MCM-41 support (**Figure S7**), confirming the catalyst integrity. However, the (100) reflection shifts slightly to higher angles, indicating the presence of smaller pore diameters, most likely due to adsorbed humins in the mesochannels. The presence of humin oligomers is confirmed by  $^{13}\text{C}$  CP/MAS NMR analysis of the spent catalyst **1** (**Figure S8**). The spectrum shows a multiplicity of bands in the range 130-190 ppm with larger bands centered at 153 and 112 ppm that can be attributed to  $\alpha$ -carbon phenol or linked furan groups, and  $\beta$ -carbon phenol or furan protonated groups, respectively [77]. Thus, humin oligomers are expected to block the propylamine sites, resulting in the observed decline of activity after the first run.

## 4. Conclusion

Along this study we studied the aldol condensation between furfural and ketones to produce high added value furan derivatives as biosolvent and biofuel precursor in the branched alkane range. In this view, a single-reactor tandem reaction based on aldol condensation/crotonization of furfural with methyl isobutyl ketone, followed by hydrogenation, was implemented. Porous organosiliceous active hybrid materials containing heterogenized amine groups and palladium nano-

particles were successfully used as bifunctional solid catalysts, in which the active sites were homogeneously distributed and stabilized in the mesochannels. The availability of amine groups grafted on the silica surface after functionalization with Pd nanoparticles was confirmed by CO<sub>2</sub> adsorption followed by FTIR spectroscopy. Operation in batch reactor afforded control the different hydrogenated products in a single-reactor tandem process by adjusting the reaction conditions. The catalyst robustness could be increased in a dual fixed-bed reactor affording a steady 20% furfural conversion for 12 h on stream with preferential formation of 1-(furan-2-yl)-5-methylhexan-3-one.

### Acknowledgements

This project has received funding from the European Union's Horizon 2020 research and innovation program under grant agreement N. 720783-MULTI2HYCAT. AE acknowledges “La Caixa” foundation for a PhD scholarship.

### References

1. J. N. Chheda J. A. Dumesic, *Catal. Today* 123 (2007) 59-70.
2. R. J. van Putten, J. C. van der Waal, E. de Jong, C. B. Rasrendra, H. J. Heeres, J. G. de Vries, *Chem. Rev.* 113 (2013) 1499-1597.
3. R. Mariscal, P. Maireles-Torres, M. Ojeda, I. Sádaba, M. López Granados, *Energy Environ. Sci.* 9 (2016) 1144-1189.
4. J. Thoen, R. Busch, Industrial Chemicals from Biomass – Industrial Concepts, in: *Biorefineries-Industrial Processes and Products: Status Quo and Future Directions*, ed B. Kamm, P. R. Gruber, M. Kamm, chapter 12, Wiley, 2005, pp 347-365.
5. A. A. Koutinas, C. Du, R. H. Wang, C. Webb, *Introduction to Chemicals from Biomass*, Wiley, Hoboken, 2008, pp. 77.
6. M. Dusselier, M. Mascal, B. F. Sels, *Top. Curr. Chem.* 353 (2014) 1-40.
7. X. Li, P. Jia, T. Wang, *ACS Catal.* 6 (2016) 7621-7640.
8. C. Xu, E. Paone, D. Rodríguez-Padrón, R. Luque, F. Mauriello, *Chem. Soc. Rev.* 49 (2020) 4273-4306.
9. M. J. Climent, A. Corma, S. Iborra, *Green Chem.* 16 (2014) 516-547.
10. G. W. Huber, J. N. Chheda, C. J. Barrett, J. A. Dumesic, *Science* 308 (2005) 1446-1450.
11. G. W. Huber, S. Iborra, A. Corma, *Chem. Rev.* 106 (2006) 4044-4098.
12. D. M. Alonso, J. Q. Bond, J. A. Dumesic, *Green Chem.* 12 (2010) 1493-1513.
13. J-P. Lange, J-P. van der Heide, J. van Buijtenen R. Price, *ChemSusChem.* 5 (2012) 150-166.

14. J. Q. Bond, A. A. Upadhye, H. Olcay, G. A. Tompsett, J. Jae, R. Xing, D. M. Alonso, D. Wang, T. Zhang, R. Kumar, A. Foster, S. M. Sen, C. T. Maravelias, R. Malina, S. R. H. Barrett, R. Lobo, C. E. Wyman, J. A. Dumesic, G. W. Huber, *Energy Environ. Sci.* 7 (2014) 1500-1523.
15. T. Komanoya, T. Kinemura, Y. Kita, K. Kamata, M. Hara, *J. Am. Chem. Soc.* 139 (2017) 11493-11499.
16. D. Chandra, Y. Inoue, M. Sasase, M. Kitano, A. Bhaumik, K. Kamata, H. Hosono, M. Hara, *Chem. Sci.* 9 (2018) 5949-5956.
17. X. Chen, L. Zhang, B. Zhang, X. Guo, X. Mu, *Water. Sci. Rep.* 6 (2016) 28558.
18. J. Zhang, Y. Liu, S. Yang, J. Wei, L. He, L. Peng, X. Tang, Y. Ni, *ACS Sust. Chem. Eng.* 8 (2020) 5584-5594.
19. G. Li, N. Li, Z. Wang, C. Li, A. Wang, X. Wang, Y. Cong, T. Zhang, *ChemSusChem.* 5 (2012) 1958-1966.
20. C. P. Jiménez-Gómez, J. A. Cecilia, C. García-Sancho, R. Moreno-Tost, P. Maireles-Torres, *ACS Sust. Chem. Eng.* 7 (2019) 7676-7685.
21. L. Bui, H. Luo, W. R. Gunther, Y. Roman-Leshkov, *Angew. Chem. Int. Ed.* 52 (2013) 8022-8025.
22. Y. Lou, S. Marinkovic, B. Estrine, W. Qiang, *ACS Omega* 5 (2020) 2561-2568.
23. N. Alonso-Fagúndez, M. L. Granados, R. Mariscal, M. Ojeda, *ChemSusChem.* 5 (2012) 1984-1990.
24. A. Patil, S. Shinde, S. Kamble, C. V. Rode, *Energy & Fuels* 33 (2019) 7466-7472.
25. J. M. Rubio-Caballero, S. Saravanamurugan, P. Maireles-Torres, A. Riisager, *Catal. Today* 234 (2014) 233-236.
26. A. Gumidyala, B. Wang, S. Crossley, *Sci. Adv.* 2 (2016) e1601072.
27. R. M. Cywar, L. Wang, E. Y-X. Chen, *ACS Sust. Chem. Eng.* 7 (2019) 1980-1988.
28. I. Sádaba, M. Ojeda, R. Mariscal, J. L. G. Fierro, M. López Granados, *Appl. Catal. B: Environ.* 101 (2011) 638-648.
29. I. Sádaba, M. Ojeda, R. Mariscal, R. Richards, M. López Granados, *Catal. Today* 167 (2011) 77-83.
30. W. Shen, G. A. Tompsett, K. D. Hammond, R. Xing, F. Dogan, C. P. Grey, W. Curtis Conner Jr, S. M. Auerbach, G. W. Huber, *Appl. Catal. A: Gen.* 392 (2011) 57-68.
31. L. Faba, E. Díaz, S. Ordóñez, *Appl. Catal. B: Environ.* 113-114 (2012) 201-211.
32. J. Yang, N. Li, G. Li, W. Wang, A. Wang, X. Wang, Y. Cong, T. Zhang, *ChemSusChem* 6 (2013) 1149-1152.
33. J. Yang, N. Li, S. Li, W. Wang, L. Li, A. Wang, X. Wang, Y. Cong, T. Zhang, *Green Chem.* 16 (2014) 4879-4884.
34. A. Philippou, M. W. Anderson, *J. Catal.* 189 (2000) 395-400.
35. O. Kikhtyanin, R. Bulanek, K. Frohlich, J. Cejka, D. Kubicka, *J. Mol. Catal. A: Gen.* 424 (2016) 358-368.
36. O. Kikhtyanin, Y. Ganjkhanelou, D. Kubicka, R. Bulanek, J. Cejka, *Appl. Catal. Gen.* 549 (2018) 8-18.
37. L. Faba, E. Díaz, S. Ordóñez, *ChemSusChem.* 6 (2013) 463-473.

38. L. Faba, E. Díaz, S. Ordóñez, *Biomass & Bioenergy* 56 (2013) 592-599.
39. O. Kikhtyanin, V. Kelbichova, D. Vitvarova, M. Kubu, D. Kubicka, *Catal. Today* 227 (2014) 154-162.
40. O. Kikhtyanin, P. Chlubna, T. Jindrova, D. Kubicka, *Dalton Trans.* 43 (2014) 10628-10641.
41. M. Su, W. Li, T. Zhang, H. Xin, S. Li, W. Fan, L. Ma, *Catal. Sci. Technol.* 7 (2017) 3555-3561.
42. Y. Jing, Y. Xin, Y. Guo, X. Liu, Y. Wang, *Chin. J. Catal.* 40 (2019) 1168-1177.
43. W. Li, M. Su, T. Zhang, Q. Ma, W. Fan, *Fuel* 237 (2019) 1281-1290.
44. H. J. Cho, D. Kim, J. Li, D. Su, B. Xu, *J. Am. Chem. Soc.* 140 (2018) 13514-13520.
45. H. J. Cho, D. Kim, B. Xu, *ACS Catal.* 10 (2020) 4770-4779.
46. C. J. Barrett, J. N. Chheda, G. W. Huber, J. A. Dumesic, *Appl. Catal. B: Environ.* 66 (2006) 111-118.
47. W. Xu, X. Liu, J. Ren, P. Zhang, Y. Wang, Y. Guo, Y. Guo, G. A. Lu, *Catal. Commun.* 11 (2010) 721-726.
48. L. Faba, E. Diaz, S. Ordóñez, *Catal. Today* 164 (2011) 451-456.
49. L. Faba, E. Diaz, S. Ordóñez, *ChemSusChem.* 7 (2014) 2816-2820.
50. M. Li, X. Xu, Y. Gong, Z. Wei, Z. Hou, H. Li, Y. Wang, *Green Chem.* 16 (2014) 4371-4377.
51. L. Gao, I. Miletto, C. Ivaldi, G. Paul, L. Marchese, S. Coluccia, F. Jiang, E. Gianotti, M. Pera-Titus, *J. Catal.* 397 (2021) 397, 75-89.
52. U. Diaz, D. Brunel, A. Corma, *Chem. Soc. Rev.* 42 (2013) 4083-4097.
53. U. Diaz, A. Corma, *Chem. Eur. J.* 24 (2018) 3944-3958.
54. A. De Vylder, J. Lauwaert, D. Esquivel, D. Poelman, J. De Clercq, P. Van Der Voort, J. W. Thybaut, *J. Catal.* 361 (2018) 51-61.
55. T. Moteki, Y. Koga M. Ogura, *J. Catal.* 378 (2019) 131-139.
56. T. Yutthalekha, D. Suttipat, S. Salakhum, A. Thivasasith, S. Nokbin, J. Limtrakul, C. Wattanakit, *Chem. Commun.* 53 (2017) 12185-12188.
57. V. M. Faria, G. A. Almeida, J. A. Mota, *Quimica Nova* 41 (2018) 601-606.
58. N. Sosa, N. Chanlek, J. Wittayakun, *Ultrason. Sonochem.* 62 (2020) 104857.
59. K. Shimizu, E. Hayashi, T. Inokuchi, T. Kodama, *Tetrahedron Lett.* 43 (2002) 9073-9075.
60. J. Hajek, M. Vandichel, B. Van de Voorde, B. Bueken, D. De Vos, M. Waroquier, V. Van Speybroeck, *J. Catal.* 331 (2015) 1-12.
61. A. Corma, U. Diaz, T. Garcia, G. Sastre, A. Velty, *J. Am. Chem. Soc.* 132 (2010) 15011-15021.
62. E. Gianotti, U. Diaz, A. Velty, A. Corma, *Catal. Sci. Technol.* 3 (2013) 2677-2688.
63. N. C. Nelson, U. Chaudhary, K. Kandel, *Top. Catal.* 57 (2014) 1000-1006.
64. A. Erigoni, M. C. Hernández-Soto, F. Rey, C. Segarra, U. Díaz, *Catal. Today* 345 (2020) 227-236.
65. J. Clayden, *Science of Synthesis*, Thieme Chemistry, 2008, vol. 36, pp. 271-341.
66. A. De Vylder, J. Lauwaert, M. K. Sabbe, M-F. Reyniers, J. De Clercq, P. Van Der Voort, J. W. Thybaut, *Catal. Today* 334 (2019) 96-103.
67. C. Ivaldi, I. Miletto, G. Paul, G. B. Giovenzana, A. Fraccarollo, M. Cossi, L. Marchese, E. Gianotti, *Molecules* (2019) 824.

68. Y. Zhao, M. Fan, P. Wang, C. Li, L. Wang L. Wang, *Fuel Process. Technol.* 198 (2020) 106250.
69. R. E. Morsi R. S. Mohamed, *R. Soc. Open Sci.* 5 (2020) 172021.
70. K-M. Li, J-G. Jiang, S-C. Tian, X-J. Chen, F. Yan, *J. Phys. Chem. C* 118 (2014) 2454-2462.
71. F. P. Miknis, D. A. Netzels, Nuclear Magnetic Resonance Characterization of Petroleum. *Encycl. Anal. Chem.* 2006 (eds. R.A. Meyers and P.A. Nick).
72. Y. S. S. Al-Faiyz, CPMAS, *Arab. J. Chem.* 10, 2017, S839-S853.
73. A. Danon, P. C. Stair, E. Weitz, *J. Phys. Chem. C* 115 (2011) 11540-11549.
74. C. Knöfel, C. Martin, V. Hornebecq, P. L. Llewellyn, *J. Phys. Chem. C* 113 (2009) 21726-21734.
75. G. Ramis, G. Busca, V. Lorenzelli, *Mater. Chem. Phys.* 29 (1991) 425-435.
76. Z. Bacsik, R. Atluri, A. E. Garcia-Bennet, N. Hedin, *Langmuir* 26 (2010) 10013-10024.
77. I. van Zandvoort, E. J. Koers, M. Weingarth, P. C. A. Bruijnincx, M. Baldus, N. M. Weckhuysen, *Green Chem.* 17 (2015) 4383-4392.

**SCHEME CAPTIONS**

**Scheme 1.** Hybrid basic catalysts **1-3** and bifunctional palladium catalyst **4**.

**Scheme 2.** Reaction scheme for aldol condensation/crotonization of FF and MIBK and potential products generated.

**Scheme 3.** Single-reactor aldol condensation/crotonization reaction of FF and MIBK, followed by hydrogenation, over catalyst **4**.

**FIGURE CAPTIONS**

**Figure 1.** (A1) Activity and pKa values of catalysts **1-3** after 24 h in the aldol condensation/ crotonization reaction of FF with MIBK; (A2) Effect of molar ratio FF/MIBK in the yield of aldol condensation/crotonization reaction between FF and MIBK; and (B) Kinetic profiles for catalyst **1**. Reaction conditions (A1,B): 1 mmol of FF, 1:4 FF/MIBK (mol/mol), 80 °C, 24 h, 5 mol% of catalyst **1** with respect to FF, 1 mmol of chlorotoluene (internal standard).

**Figure 2.** FF conversion in dual fixed-bed reactor with catalysts **1** and **4** in a fixed-bed reactor for the tandem aldol condensation/crotonization-hydrogenation reactions of FF and MIBK. Reaction conditions: 1:2 FF/MIBK (mol/mol), 1:9 MIBK/toluene (mol/mol), 80-100 °C, 12 h, 1.5 mL/h feed flow rate, 1-2 mL(STP)/min H<sub>2</sub> flowrate, WHSV = 0.23-0.35 h<sup>-1</sup>; <sup>a</sup> 300 mg cat **1**; <sup>b</sup> 150 mg cat **1** + 150 mg cat **4**; <sup>c</sup> 300 mg cat **1** + 150 mg cat **4**.

**Figure 3.** Selectivity of tandem reaction of FF and MIBK (condensation + hydrogenation) with catalysts **1** and **4** in dual fixed bed reactor with (A) 1 mL(STP)/min H<sub>2</sub> and (B) 1.5 mL(STP)/min H<sub>2</sub> (B). Other reaction conditions: FF:MIBK 1:2 (mol/mol), MIBK:Toluene 1:9 (mol/mol), 100 °C, 1.5 mL/h feed rate, 150 mg catalyst **1** + 150 mg catalyst **4**, WHSV = 0.23 h<sup>-1</sup>.

**Figure 4.** XRD patterns of catalysts **1-3**, and bifunctional palladium catalyst **4**.

**Figure 5.** (A) N<sub>2</sub> adsorption-desorption isotherms at 77 K and (B) BJH pore size distributions of catalysts **1-4** and MCM-41 support.

**Figure 6.** TGA and DTA profiles of the catalysts **1-3**.

**Figure 7.** Solid-state <sup>13</sup>C CP/MAS NMR spectra of catalysts **1-3** (bottom) and Pd-loaded catalyst **4** (top).

**Figure 8.** FTIR difference spectra of catalyst **1** (A) and catalyst **4** (B) upon CO<sub>2</sub> adsorption (curves a-d: 20, 10, 5, 1 mbar) and CO<sub>2</sub> outgassing at room temperature (curves e). Curve  $\alpha$  in Section A: CO<sub>2</sub> (20 mbar) adsorbed on the pristine MCM-41.

**Figure 9.** HR-TEM micrographs of catalyst **4** recorded in bright-field (A-B) and dark-field (C) modes. Particle size distribution calculated upon measuring the size of 148 particles over a total of six micrographs (D).

**TABLE CAPTIONS**

**Table 1.** Physicochemical and textural properties of hybrid catalysts **1-4** and MCM-41 support.



**Table 2.** Influence of the operation conditions on the catalytic properties of catalyst **1\*** in the aldol condensation/crotonization reaction between FF and MIBK. The ALD-1 selectivity was 100% in all experiments.

**Table 3.** Catalytic activity of catalyst **4** for the tandem reaction between FF and MIBK<sup>a</sup>

**Table 1.** Physicochemical and textural properties of hybrid catalysts **1-4** and MCM-41 support

Catalyst	N / wt% <sup>a</sup>	C / wt% <sup>a</sup>	WL / wt% <sup>b</sup>	Pd / wt% <sup>c</sup>	SSA <sub>BET</sub> (m <sup>2</sup> g <sup>-1</sup> ) <sup>d</sup>	Pore size (Å) <sup>d</sup>	Pore volume (cm <sup>3</sup> g <sup>-1</sup> ) <sup>d</sup>	S <sub>micro</sub> (m <sup>2</sup> g <sup>-1</sup> ) <sup>d</sup>	N surface density <sup>e</sup>
Cat. <b>1</b>	1.1	3.3	4.4	-	973	25	0.47	3.3	0.49
Cat. <b>2</b>	2.4	5.8	8.2	-	1159	24	0.55	24	0.44
Cat. <b>3</b>	2.5	7.9	10.4	-	1005	22	0.43	67	0.36
Cat. <b>4</b>	1.3	8.8	10.0	0.8	913	24	0.13	0	0.61
MCM-41	-	-	-	-	1064	27	0.81	0	-

<sup>a</sup> Measured by elemental analysis; <sup>b</sup> measured by TGA (WL = total weight loss); <sup>c</sup> measured by ICP-OES; <sup>d</sup> measured from N<sub>2</sub> adsorption-desorption isotherms at -196 °C; atoms of N/nm<sup>2</sup>.

**Table 2.** Influence of the operation conditions on the catalytic properties of catalyst **1**\* in the aldol condensation/crotonization reaction between FF and MIBK. The ALD-1 selectivity was 100% in all experiments.

Entry	Temperature (°C)	Catalyst (wt%)	Solvent (g)	ALD-1 yield (%)	ALD-1 yield (re-use) (%)
1	80 °C	5	-	56	<5
2	80 °C	5	0.5	52	<15 <sup>a</sup>
3	80 °C	5	1.0	30	<15 <sup>a</sup>
4	80 °C	10	0.5	89	23 <sup>b</sup>
5	80 °C	10	0.5	99	23 <sup>c</sup>
6	80 °C	10	1.0	74	32 <sup>a</sup>
7	100 °C	10	0.5	99	25 <sup>e</sup>
8	100 °C	10	1.0	95	24 <sup>d</sup>

\* Reaction conditions: 1 mmol of FF, 1:2 FF/MIBK (mol/mol), 24 h, toluene, 1 mmol of 4-chlorotoluene (internal standard).

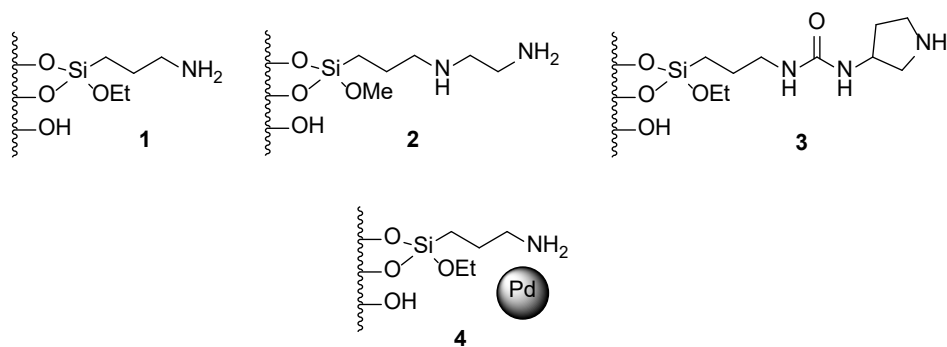
<sup>a</sup> Washed with acetone at 40 °C; <sup>b</sup> washed with toluene at 60 °C; <sup>c</sup> washed with DMSO at RT; <sup>d</sup> washed with acetone at room temperature; <sup>e</sup> washed with acetone for 30 min at RT.

**Table 3.** Catalytic activity of catalyst **4** for the tandem reaction between FF and MIBK<sup>a</sup>

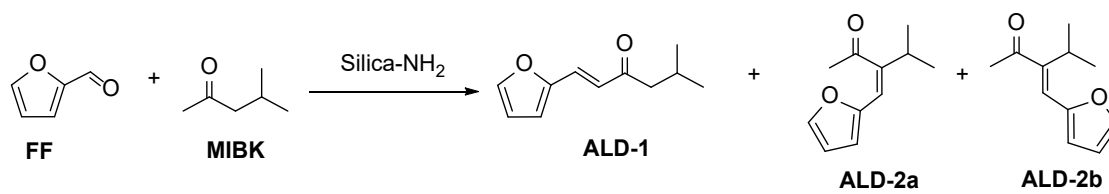
En-try	Reaction conditions		FF conver-sion (%)	Yield (%)		
	Step 1	Step 2		F-ALD-1-ON	F-ALD-1-OL	F-ALD-1-AN
<b>1</b>	80 °C; 24 h	80 °C; 8 h, 5 bar H <sub>2</sub>	75	21	10	44
<b>2<sup>d</sup></b>	80 °C; 24 h	80 °C; 24 h, 5 bar H <sub>2</sub>	48	12	12	23
<b>3<sup>b</sup></b>	80 °C; 24 h	80 °C; 24 h, 5 bar H <sub>2</sub>	65	6	29	30
<b>4</b>	80 °C; 24 h	80 °C; 24 h, 5 bar H <sub>2</sub>	57	1	18	38
<b>5</b>	100 °C; 24 h	100 °C; 8 h, 5 bar H <sub>2</sub>	80	63	7	10
<b>6<sup>c</sup></b>	100 °C; 24 h	100 °C; 8 h, 5 bar H <sub>2</sub>	96	44	9	47
<b>7</b>	100 °C; 24 h	100 °C; 24 h, 5 bar H <sub>2</sub>	94	3	15	82

<sup>a</sup> Reaction conditions: 1 mmol of FF, 1:2 FF/MIBK (mol:mol), 0.5 g toluene; <sup>b</sup> 1:4 FF/MIBK (mol:mol); <sup>c</sup> 1:6 FF/MIBK and no toluene; <sup>d</sup> 5 mol<sub>N</sub>% catalyst **1** with respect to FF.

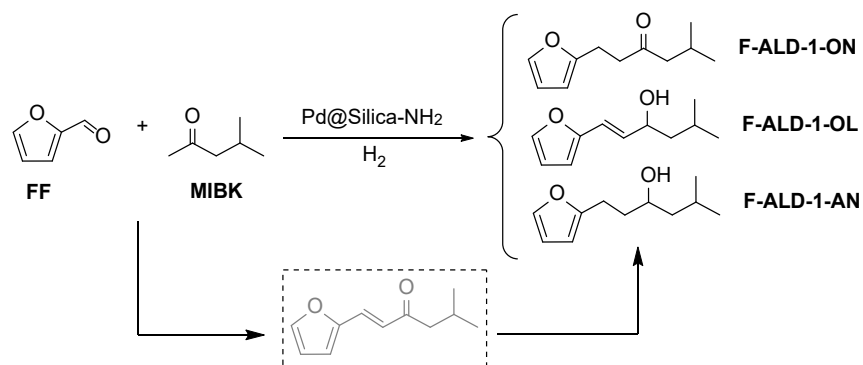
## SCHEMES



**Scheme 1.** Hybrid basic catalysts **1-3** and bifunctional palladium catalyst **4**.



**Scheme 2.** Reaction scheme for aldol condensation/crotonization of FF and MIBK and potential products generated.



**Scheme 3.** Single-reactor aldol condensation/crotonization reaction of FF and MIBK, followed by hydrogenation, over catalyst **4**.

## FIGURES

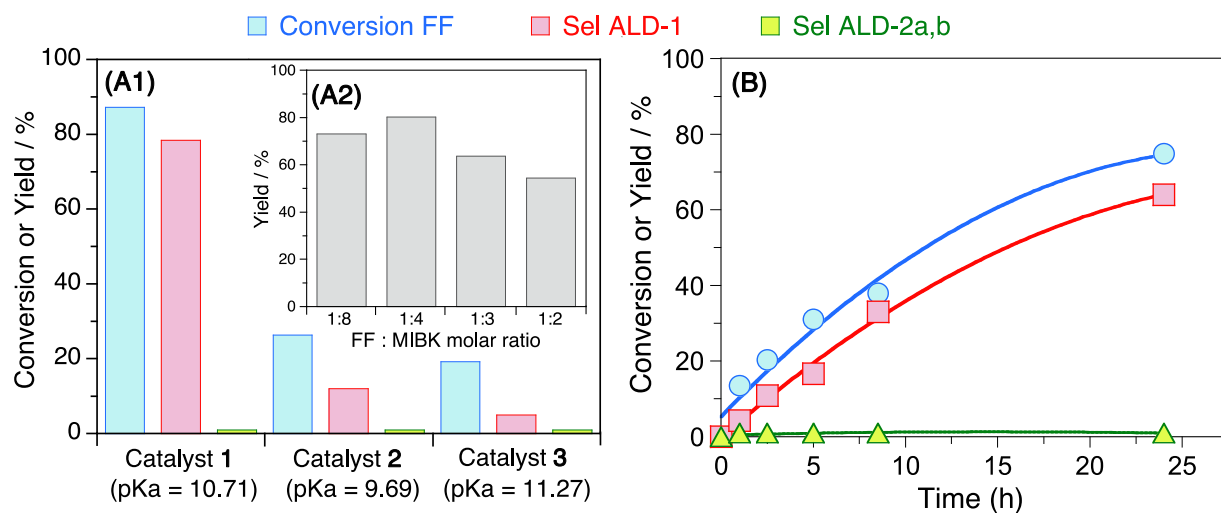


**Figure 1.** (A1) Activity and pKa values of catalysts **1-3** after 24 h in the aldol condensation/ crotonization reaction of FF with MIBK; (A2) Effect of molar ratio FF/MIBK in the yield of aldol condensation/crotonization reaction between FF and MIBK; and (B) Kinetic profiles for catalyst **1**. Reaction conditions (A1,B): 1 mmol of FF, 1:4 FF/MIBK (mol/mol), 80 °C, 24 h, 5 mol<sub>N</sub>% of catalyst **1** with respect to FF, 1 mmol of chlorotoluene (internal standard).



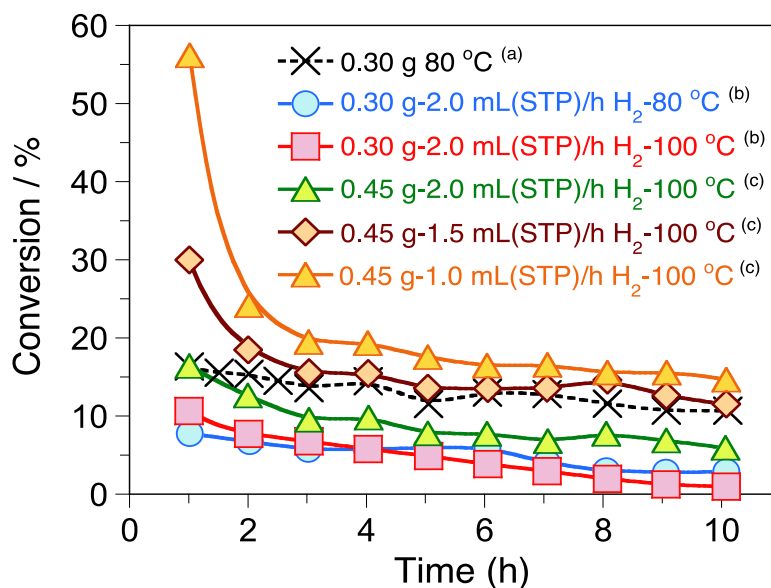


**Figure 2.** FF conversion in dual fixed-bed reactor with catalysts **1** and **4** in a fixed-bed reactor for the tandem aldol condensation/crotonization-hydrogenation reactions of FF and MIBK. Reaction conditions: 1:2 FF/MIBK (mol/mol), 1:9 MIBK/toluene (mol/mol), 80-100 °C, 12 h, 1.5 mL/h feed flow rate, 1-2 mL(STP)/min H<sub>2</sub> flowrate, WHSV = 0.23-0.35 h<sup>-1</sup>; <sup>a</sup> 300 mg cat **1**; <sup>b</sup> 150 mg cat **1** + 150 mg cat **4**; <sup>c</sup> 300 mg cat **1** + 150 mg cat **4**.

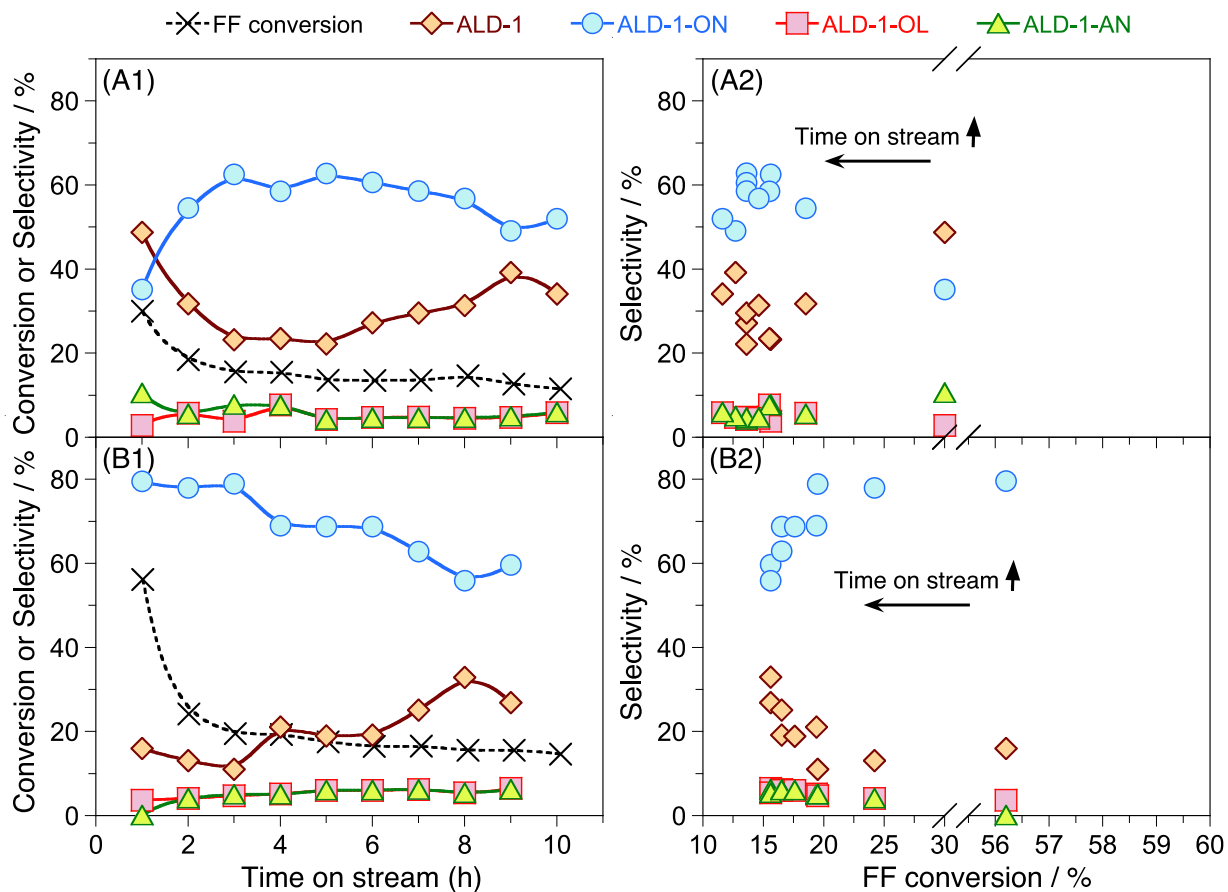


**Figure 3.** Selectivity of tandem reaction of FF and MIBK (condensation + hydrogenation) with catalysts **1** and **4** in dual fixed bed reactor with (A) 1 mL(STP)/min H<sub>2</sub> and (B) 1.5 mL(STP)/min H<sub>2</sub> (B). Other reaction conditions: FF:MIBK 1:2 (mol/mol), MIBK:Toluene 1:9 (mol/mol), 100 °C, 1.5 mL/h feed rate, 300 mg catalyst **1** + 150 mg catalyst **4**, WHSV = 0.23 h<sup>-1</sup>.

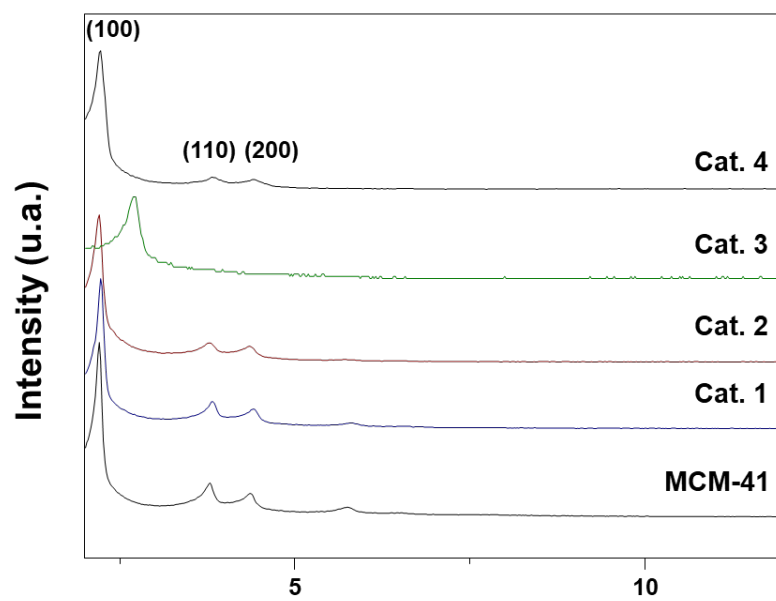


**Figure 4.** XRD patterns of catalysts **1-3**, and bifunctional palladium catalyst **4**.

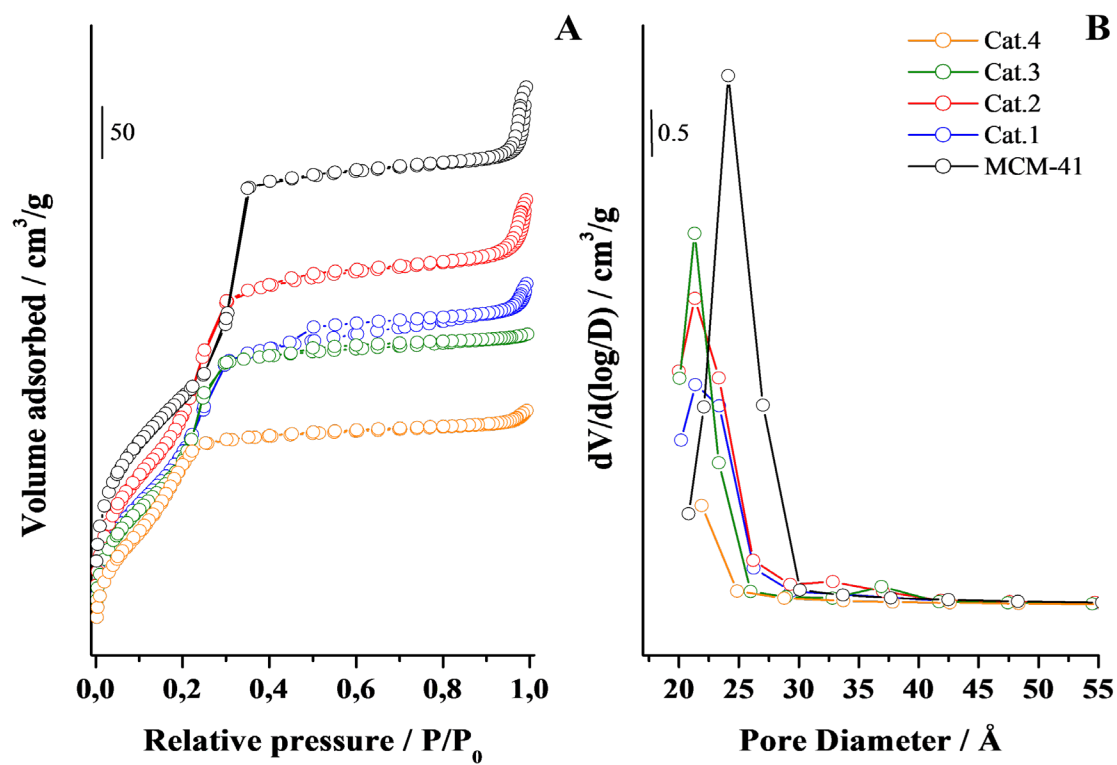


**Figure 5.** (A) N<sub>2</sub> adsorption-desorption isotherms at 77 K and (B) BJH pore size distributions of catalysts 1-4 and MCM-41 support.

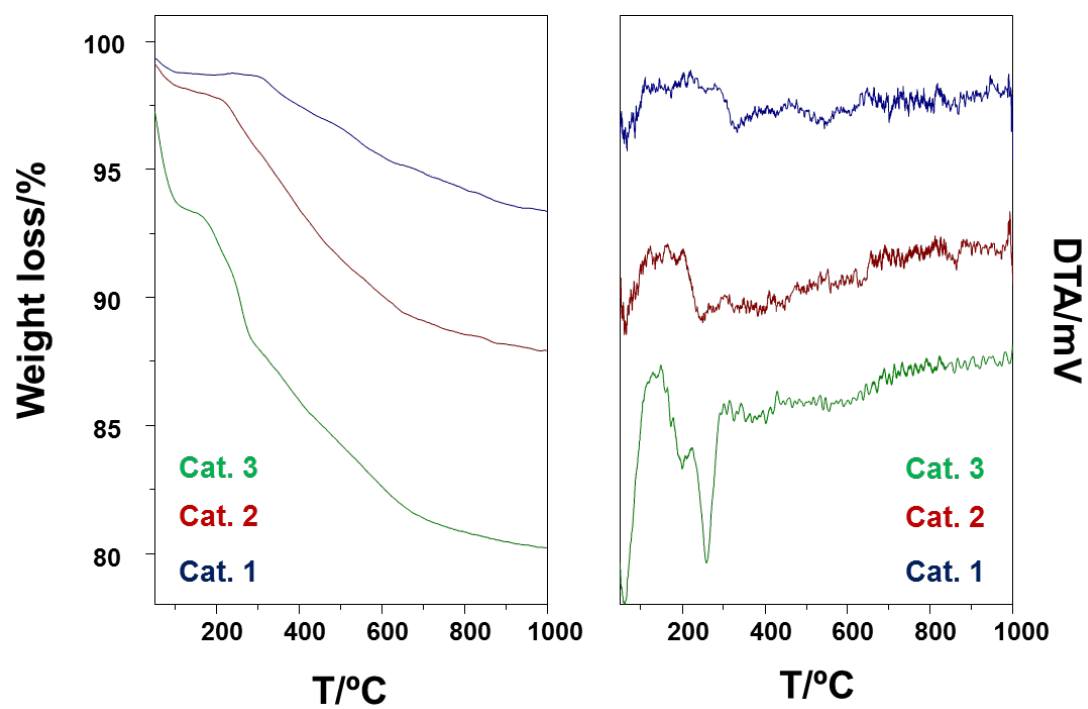
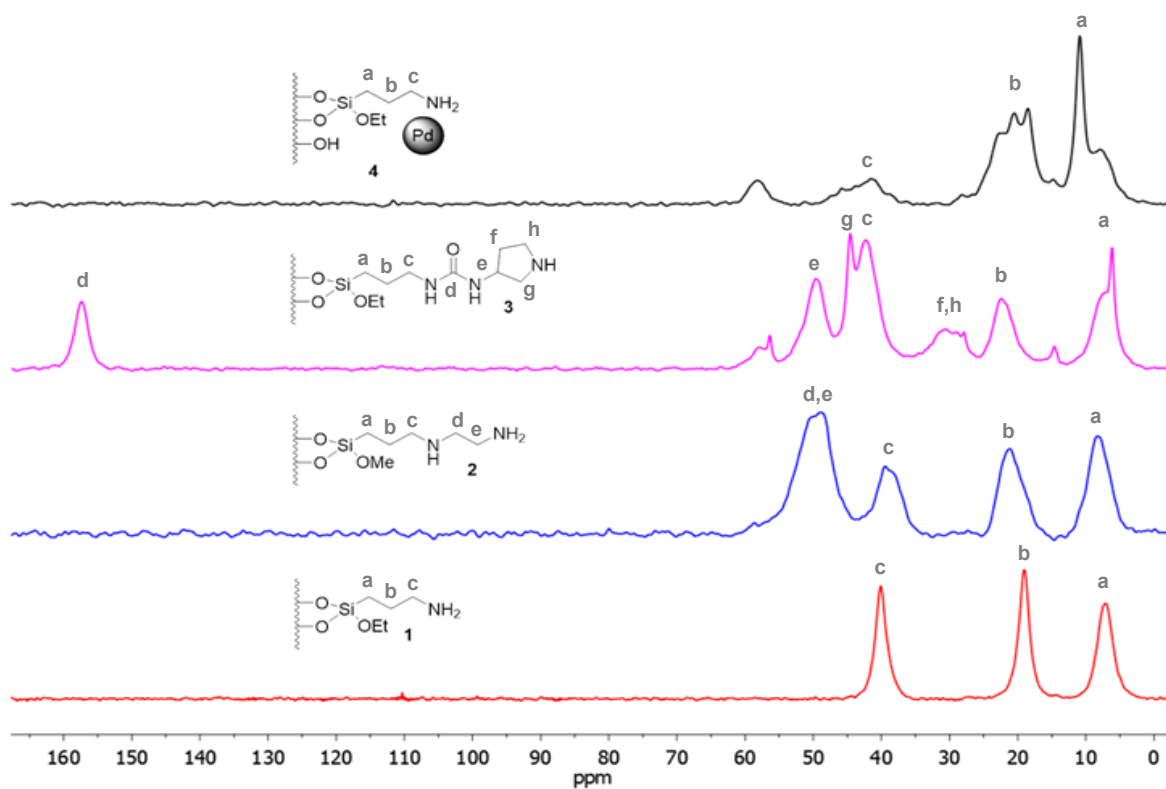
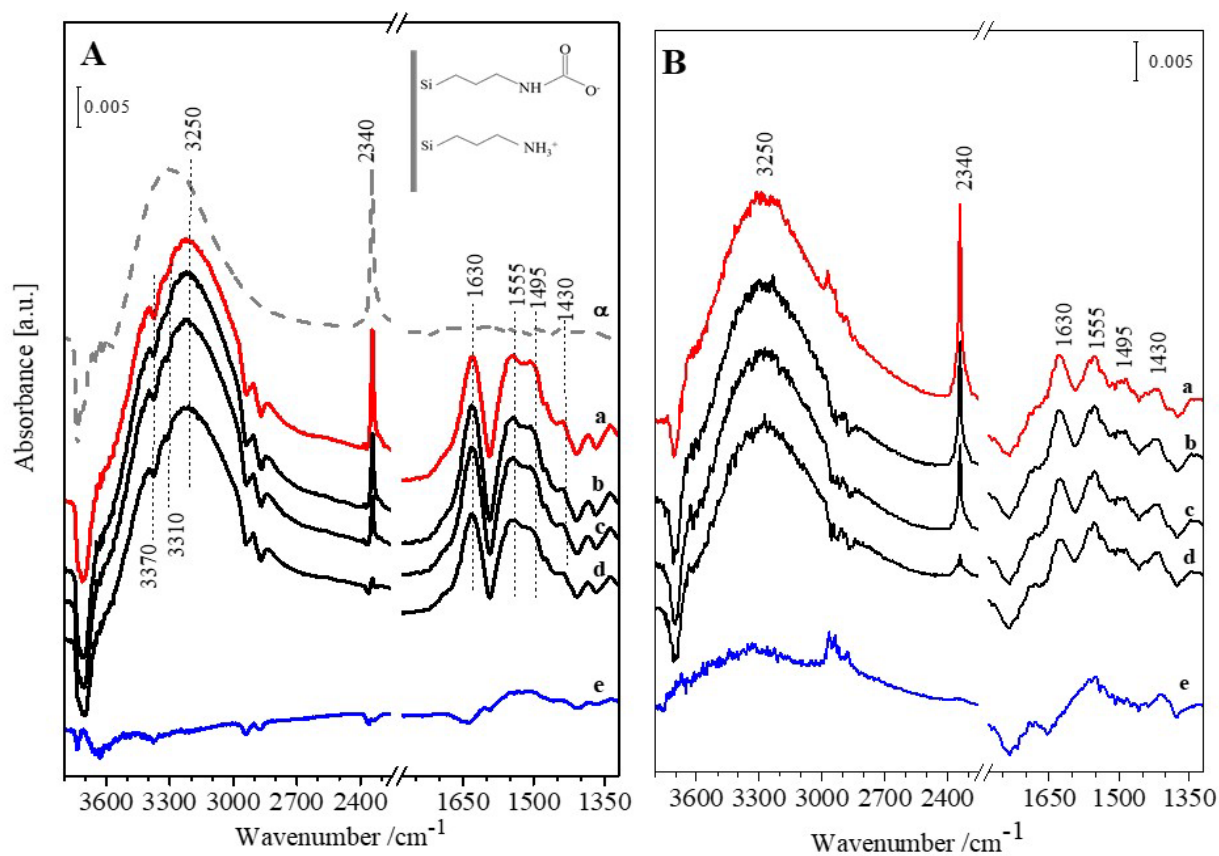


Figure 6. TGA and DTA profiles of the catalysts 1-3.



**Figure 7.** Solid-state  $^{13}\text{C}$  CP/MAS NMR spectra of catalysts 1-3 (bottom) and Pd-loaded catalyst 4 (top).



**Figure 8.** FTIR difference spectra of catalyst 1 (A) and catalyst 4 (B) upon CO<sub>2</sub> adsorption (curves a-d: 20, 10, 5, 1 mbar) and CO<sub>2</sub> outgassing at room temperature (curves e). Curve  $\alpha$  in Section A: CO<sub>2</sub> (20 mbar) adsorbed on the pristine MCM-41.

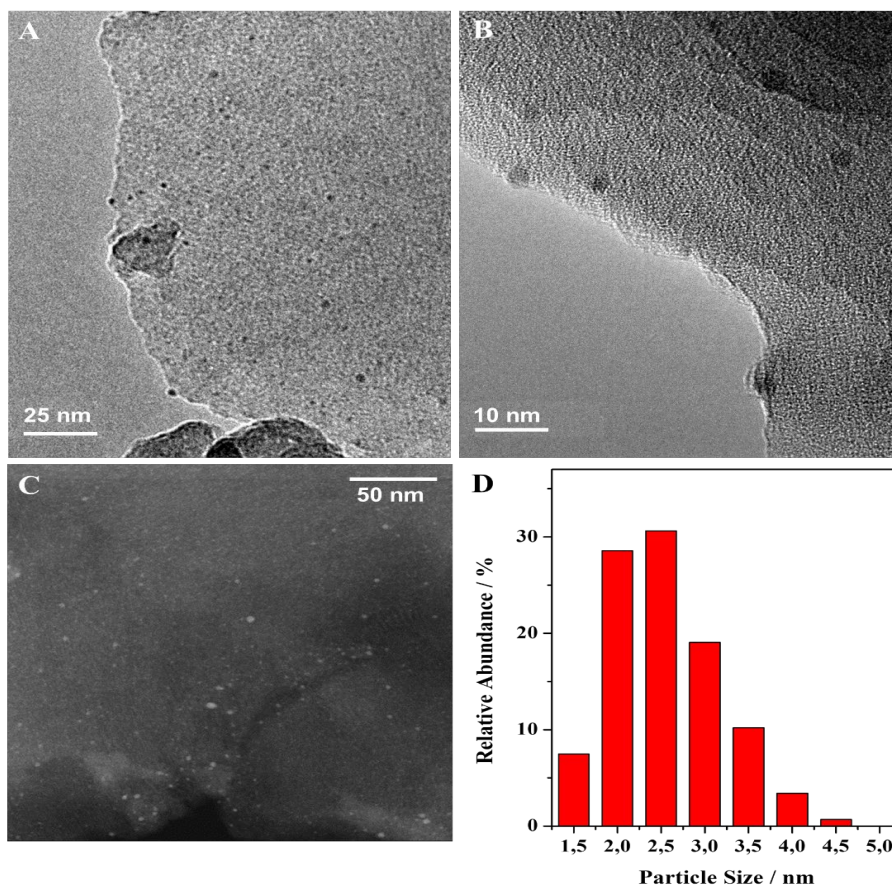


**Figure 9.** HR-TEM micrographs of catalyst **4** recorded in bright-field (A-B) and dark-field (C) modes. Particle size distribution calculated upon measuring the size of 148 particles over a total of six micrographs (D).



**Table 1.** Physicochemical and textural properties of hybrid catalysts **1-4** and MCM-41 support

Catalyst	N / wt% <sup>a</sup>	C / wt% <sup>a</sup>	WL / wt% <sup>b</sup>	Pd / wt% <sup>c</sup>	SSA <sub>BET</sub> (m <sup>2</sup> g <sup>-1</sup> ) <sup>d</sup>	Pore size (Å) <sup>d</sup>	Pore volume (cm <sup>3</sup> g <sup>-1</sup> ) <sup>d</sup>	S <sub>micro</sub> (m <sup>2</sup> g <sup>-1</sup> ) <sup>d</sup>	N surface density <sup>e</sup>
Cat. <b>1</b>	1.1	3.3	4.4	-	973	25	0.47	3.3	0.49
Cat. <b>2</b>	2.4	5.8	8.2	-	1159	24	0.55	24	0.44
Cat. <b>3</b>	2.5	7.9	10.4	-	1005	22	0.43	67	0.36
Cat. <b>4</b>	1.3	8.8	10.0	0.8	913	24	0.13	0	0.61
MCM-41	-	-	-	-	1064	27	0.81	0	-

<sup>a</sup> Measured by elemental analysis; <sup>b</sup> measured by TGA (WL = total weight loss); <sup>c</sup> measured by ICP-OES; <sup>d</sup> measured from N<sub>2</sub> adsorption-desorption isotherms at -196 °C; atoms of N/nm<sup>2</sup>.


**Table 2.** Influence of the operation conditions on the catalytic properties of catalyst **1**\* in the aldol condensation/crotonization reaction between FF and MIBK. The ALD-1 selectivity was 100% in all experiments.

Entry	Temperature (°C)	Catalyst (wt%)	Solvent (g)	ALD-1 yield (%)	ALD-1 yield (re-use) (%)
1	80 °C	5	-	56	<5
2	80 °C	5	0.5	52	<15 <sup>a</sup>
3	80 °C	5	1.0	30	<15 <sup>a</sup>
4	80 °C	10	0.5	89	23 <sup>b</sup>
5	80 °C	10	1.0	74	32 <sup>a</sup>
<b>6</b>	<b>100 °C</b>	<b>10</b>	<b>0.5</b>	<b>99</b>	<b>23<sup>c</sup></b>
7	100 °C	10	0.5	99	25 <sup>d</sup>
8	100 °C	10	1.0	95	24 <sup>e</sup>

\* Reaction conditions: 1 mmol of FF, 1:2 FF/MIBK (mol/mol), 24 h, toluene, 1 mmol of 4-chlorotoluene (internal standard).

<sup>a</sup> Washed with acetone at 40 °C; <sup>b</sup> washed with toluene at 60 °C; <sup>c</sup> washed with DMSO at RT; <sup>d</sup> washed with acetone for 30 min at RT; <sup>e</sup> washed with acetone at room temperature.

**Table 3.** Catalytic activity of catalyst **4** for the tandem reaction between FF and MIBK<sup>a</sup>

Entry	Reaction conditions		FF conversion (%)	Yield (%)		
	Step 1	Step 2		F-ALD-1-ON	F-ALD-1-OL	F-ALD-1-AN
<b>1</b>	80 °C; 24 h	80 °C; 8 h, 5 bar H <sub>2</sub>	75	21	10	44
<b>2<sup>b</sup></b>	80 °C; 24 h	80 °C; 24 h, 5 bar H <sub>2</sub>	48	12	12	23
<b>3<sup>c</sup></b>	80 °C; 24 h	80 °C; 24 h, 5 bar H <sub>2</sub>	65	6	29	30
<b>4</b>	80 °C; 2448 h, 5 bar H <sub>2</sub>	80 °C; 24 h, 5 bar H <sub>2</sub>	57	1	18	38
<b>5</b>	100 °C; 24 h	100 °C; 8 h, 5 bar H <sub>2</sub>	80	63	7	10
<b>6<sup>d</sup></b>	100 °C; 24 h	100 °C; 8 h, 5 bar H <sub>2</sub>	96	44	9	47
	100 °C; 2448 h, 5 bar H <sub>2</sub>	100 °C; 24 h, 5 bar H <sub>2</sub>	94	3	15	82

<sup>a</sup> Reaction conditions: 1 mmol of FF, 1:2 FF/MIBK (mol:mol), 0.5 g toluene; <sup>b</sup> 1:4 FF/MIBK (mol:mol); <sup>c</sup> 1:6 FF/MIBK and no toluene; <sup>d</sup> 5 mol<sub>N</sub>% catalyst **1** with respect to FF.

<sup>a</sup> Reaction conditions: 1 mmol of FF, 1:2 FF/MIBK (mol:mol), 0.5 g toluene; <sup>b</sup> 5 mol<sub>N</sub>% catalyst **1** with respect to FF; <sup>c</sup> 1:4 FF/MIBK (mol:mol); <sup>d</sup> 1:6 FF/MIBK and no toluene.